nature communications

Article

https://doi.org/10.1038/s41467-025-66041-y

Ligand-channel-induced ion liberation in crowded zwitterionic hydrogel electrolyte for efficient zinc metal batteries

Received: 30 November 2024

Accepted: 29 October 2025

Published online: 11 December 2025

Check for updates

Cheng Wang[1,2,5], Zhe Gong[1,5], Jodie A. Yuwono[2,5], Qiangqiang Meng[3], Yanqiu Lyu[2], Shilin Zhang[2], Shuixin Xia[2], Xin Zeng[1], Patrick J. Cullen[1], Jianfeng Mao[2] ✉, Zaiping Guo[2,4] ✉ & Zengxia Pei[1] ✉

Developing efficient electrolytes is vital for realizing the vision of aqueous rechargeable zinc-metal batteries as a safe and sustainable energy storage technology. Emerging electrolyte engineering approaches including concentrated and molecular crowding electrolytes restrict water reactivity but usually incur limited bulk ionic conductivity and sluggish interfacial kinetics as well. Here we show that this dilemma can be addressed by deploying hydrogel electrolytes that incorporate typical molecular crowding electrolytes with a zwitterionic polymer matrix. This crowded zwitterionic hydrogel electrolyte counterintuitively entails Zn^{2+} liberation for higher ionic conductivity and prompt interfacial desolvation kinetics while maintaining essential advantages of molecular crowding electrolytes, thereby fundamentally overcoming the critical issues associated with such electrolytes. Such electrolytes enable the assembled zinc-metal batteries and zinc-ion hybrid capacitors to work effectively and stably at high rates (up to 5 A g^{-1}) and frozen temperatures (down to −60°C). The applicability of this crowding-induced ion liberation strategy was also extended to other aqueous metal-ion (Mg^{2+} and Na^{+}) batteries. This work has the potential to provide a general solution to efficient electrolytes for safer, energy-dense, and cost-effective aqueous energy storage technologies.

The rapid technological progress of renewable electricity necessitates commensurate energy storage systems (ESSs). Citing concerns over safety and cost, traditional lithium-ion batteries fall short in meeting the requirements of the grid-scale ESSs. Rechargeable zinc-metal batteries (RZMBs) emerged as such a promising and sustainable alternative, merited by their intrinsic safety, low-cost, and easy manufacturing[1–4]. Though the batteries' aqueous nature is central to these advantages, it concomitantly restricts the electrochemical voltage window and interfacial stability of the electrodes in RZMBs. These problems mainly stem from the high reactivity of essential water species within the electrolyte, posing major hurdles for the eventual applications of RZMBs[2,5–9]. For example, excess free water molecules easily decompose and dissolve electrode materials, whilst solvated water species can corrode Zn negative electrode, aggravate dendrite formation, and incur high desolvation barriers[10,11]. In this context, electrolyte engineering strategies including concentrated "water-in-salt" (WIS), hybrid-solvent, and "molecular crowding" electrolytes have been vibrantly scrutinized, with great strides realized in the last few years[3,10,12–15]. Nevertheless, WIS electrolytes deploy excess salts that inevitably cause safety (particularly for fluorine-containing

[1]School of Chemical and Biomolecular Engineering, The University of Sydney, Sydney, NSW, Australia. [2]School of Chemical Engineering, The University of Adelaide, Adelaide, SA, Australia. [3]School of Physics and Materials Engineering, Hefei Normal University, Hefei, China. [4]Department of Materials Science and Engineering, City University of Hong Kong, Kowloon, Hong Kong, China. [5]These authors contributed equally: Cheng Wang, Zhe Gong, Jodie A. Yuwono. ✉e-mail: jianfeng.mao@adelaide.edu.au; zaipiguo@cityu.edu.hk; zengxia.pei@sydney.edu.au

electrolytes) and cost concerns, contradicting the innate advantages of RZMBs. Worse still, while effective in widening voltage window and stabilizing electrodes, these electrolytes always engender low bulk ionic conductivity and sluggish interfacial desolvation kinetics that hurdle RZMBs' realistic rate performance and low-temperature adaptability[16].

Another strategy with growing interest is deploying polymer matrices to fabricate hydrogel electrolytes (HEs), which feature liquid-like ion transport diffusivity and solid-like cohesive integrity. These HEs entrap water with tunable hydrogen-bonding and/or ion-dipole interactions, thereby circumventing the leakage issues and offering an alternative approach to alleviate the water-relevant side reactions[17–19]. Nonetheless, these advantages are still at the expense of conductivity and kinetics compared to those of their liquid counterparts, given that the water-binding hydrophilic nature of the gel backbone impedes the transport of cations as well[20]. This is particularly pronounced for viscous solutes that have fewer side reactions, such as concentrated or crowded electrolytes. To increase ionic conductivity and interfacial kinetics, a common strategy is to introduce a large amount of water into the gel, which in turn spawns side reactions and limits the electrochemical window. This dilemma underscores the critical importance of hydrogel matrix design for the delicate balance of the water-ion-polymer nexus. Recently, zwitterionic (Zw) small molecules or polymers with "inner salt" dissociation properties have been proven to improve the dissociation of target salt species and form somehow aligned ion channels, thereby enhancing the ionic conductivity of the corresponding electrolytes[21–24]. Despite these advances, the overall impact and general applicability of Zw matrices on cation liberation, including conductivity, transference number, interfacial kinetics, and Zn negative electrode interface regularity, remain obscure. Therefore, addressing this knowledge gap is essential to fully leverage suitable HEs for realizing the full potential of RZMBs.

In this work, we demonstrated that a Zw hydrogel matrix can counterintuitively enable Zn^{2+} liberation in a molecular-crowded electrolyte. The Zw gel was chosen over other conventional polymer matrices (e.g., polyvinyl alcohol, polyacrylamide) due to its inner-salt structure, which holds potential to facilitate ion transport. Among various molecular crowding agents, disaccharides (such as maltose, sucrose) were chosen due to their strong covalent-like hydrogen bonding capability, which bridges polymer networks and effectively immobilizes water molecules, enhancing electrolyte performance and stability[25,26]. With the dual-induction effect of concentrated maltose molecules in bridging both ions and polymer chains, the ion-water-polymer interactions in the Zw HE were finely tuned. Combined spectroscopic studies with molecular-scale modeling reveal that the Zn^{2+} carriers feature less solvation water and fewer contact ion pairs (CIPs), thus are liberated to migrate more efficiently along the Zw polymer ion channel and better desolvate for interfacial reactions. As such, the crowded Zw HE provides an ionic conductivity comparable to or higher than that of the liquid equivalent, a wider electrochemical window (2.6 V), stable and reversible Zn negative electrode interfaces at high utilizations (up to 57%), and good temperature adaptability. This HE sustains the assembled RZMBs and hybrid capacitors working stably at high rates and low temperatures (down to −60 °C). Further, the universality of this crowding-induced ion liberation strategy was validated in other aqueous metal-ion (Mg^{2+} and Na^{+}) batteries, presenting new opportunities to innovate energy-dense, low-cost, and safe energy storage technologies.

Results

Promotion of Zn^{2+} migration by enhanced ion-polymer interactions in crowded Zw gel electrolyte

The water species within the hydrogel network can be classified into bound water, intermediate water, and free water[27]. Bound water refers to those firmly bound to the hydrophilic polymer network by hydrogen bonding or electrostatic forces. Intermediate water is immediately adjacent to bound water but interacts with adjacent water or polymer networks with less than four hydrogen bonds. Free water interacts negligibly with the gel polymer chains[17]. Given the high polarity and dielectric constant of water, it can easily solvate most typical zinc salts. However, at low concentration, the zinc salts will dominantly dissociate in the free water moiety of HEs, with weak (or even negligible) interactions between solvated ions and the gel polymer chains (illustrated in Fig. 1a, c). In this scenario, the electrochemical behavior of ions in the HE more resembles their liquid equivalents, easily causing premature failure of the batteries.

To enhance the polymer-ion interactions, we deployed a dual-induction strategy at the molecular level by introducing maltose into the Zw HE, as illustrated in Fig. 1b. These disaccharide molecules can induce strong covalent-like hydrogen bonding between their -OH groups and the polar groups on the gel chains[26], thereby holding together the cross-linked polymer chains in the hydrogel network (illustrated in Fig. 1d). Meanwhile, the introduced maltose molecules essentially crowd the dilute salt species (exemplified by 3 m $Zn(ClO_4)_2$ here) by stabilizing excess free water[25]. More significantly, as unraveled below, these maltose molecules can substantiate gel backbone's charged groups to interact with dissociated anions and cations, inducing ion migration through the otherwise inaccessible transport avenues in the Zw polymer chains (illustrated in Fig. 1e).

To validate polymer-ion interactions from the dual-induction strategy, we first compared Raman spectra of the serial crowded Zw hydrogel electrolytes (CZHEs) and the liquid electrolyte (LE) counterparts, both are comprised of 3 m $Zn(ClO_4)_2$ plus n wt% maltose (n = 0 to 40, wt% of maltose in solution). Figure 2a and Supplementary Fig. 1 present the Raman spectra of the serial LEs. The three peaks at 464, 631, and 934 cm^{-1} correspond to the $\upsilon 2$, $\upsilon 4$, and $\upsilon 1$ vibrational modes of ClO_4^-, respectively[28,29]. As maltose concentration increased to 40 wt%, these peaks remained almost identical full widths at half maximum (FWHMs) and relative peak intensities. However, the reversed intensity of the increased $\upsilon_{C\text{-}H}$ stretch band and the decreased $\upsilon_{O\text{-}H}$ band (Supplementary Fig. 1c) suggests that the added maltose indeed breaks the tetrahedral structure and restricts the activity of water molecules[25]. These results suggest the ClO_4^- ions are barely affected in LEs, though the electrolytes have been effectively crowded. The deconvoluted spectra of the water species further reveal the obviously reduced oscillation of fully four-hydrogen bonded water (viz., free water, at *ca.* 3250 cm^{-1}) molecules (Supplementary Fig. 1d, e), resulting from the perturbation of the water hydrogen bonding network through the water-maltose interactions. These results are in line with the general expectations of "molecular crowding" electrolyte[13], indicating that maltose can increase electrochemical stability of the electrolyte.

When incorporated with the Zw hydrogel matrix, however, the ClO_4^- ions show distinct peak features within the crowded electrolyte environment (Fig. 2b, c). Specifically, in contrast to the constant band signals from the Zw backbone (~ 810 and ~1020 cm^{-1}), FWHMs and relative peak intensities of ClO_4^- ions' bands ($\upsilon 1$, $\upsilon 2$, $\upsilon 4$) decreased significantly with increasing maltose concentration (Fig. 2b, Supplementary Fig. 2). Such an evolution trend is more clearly seen by benchmarking the areas of the ClO_4^- ion's three bands with those of the Zw backbone as a reference, which displayed gradually declining ion-to-backbone ratios with higher maltose concentrations (Supplementary Figs. 3, 4). The decline in relative peak intensities indicates that the relative components surrounding ClO_4^- changed as the maltose concentration increased[30]. Considering the liquid crowding electrolyte does not show such changes (Fig. 2a), and the ClO_4^- is a well-known "salt-in" anion that has certain interactions with polymer matrix[31], this phenomenon is reasonably caused by the induction effect of maltose that prompts ClO_4^- ions to interact intensely with the Zw backbone. Meanwhile, the reduction of FWHMs (Fig. 2d, e) substantiates that the disordering of ClO_4^- collectively escalates,

https://doi.org/10.1038/s41467-025-66041-y

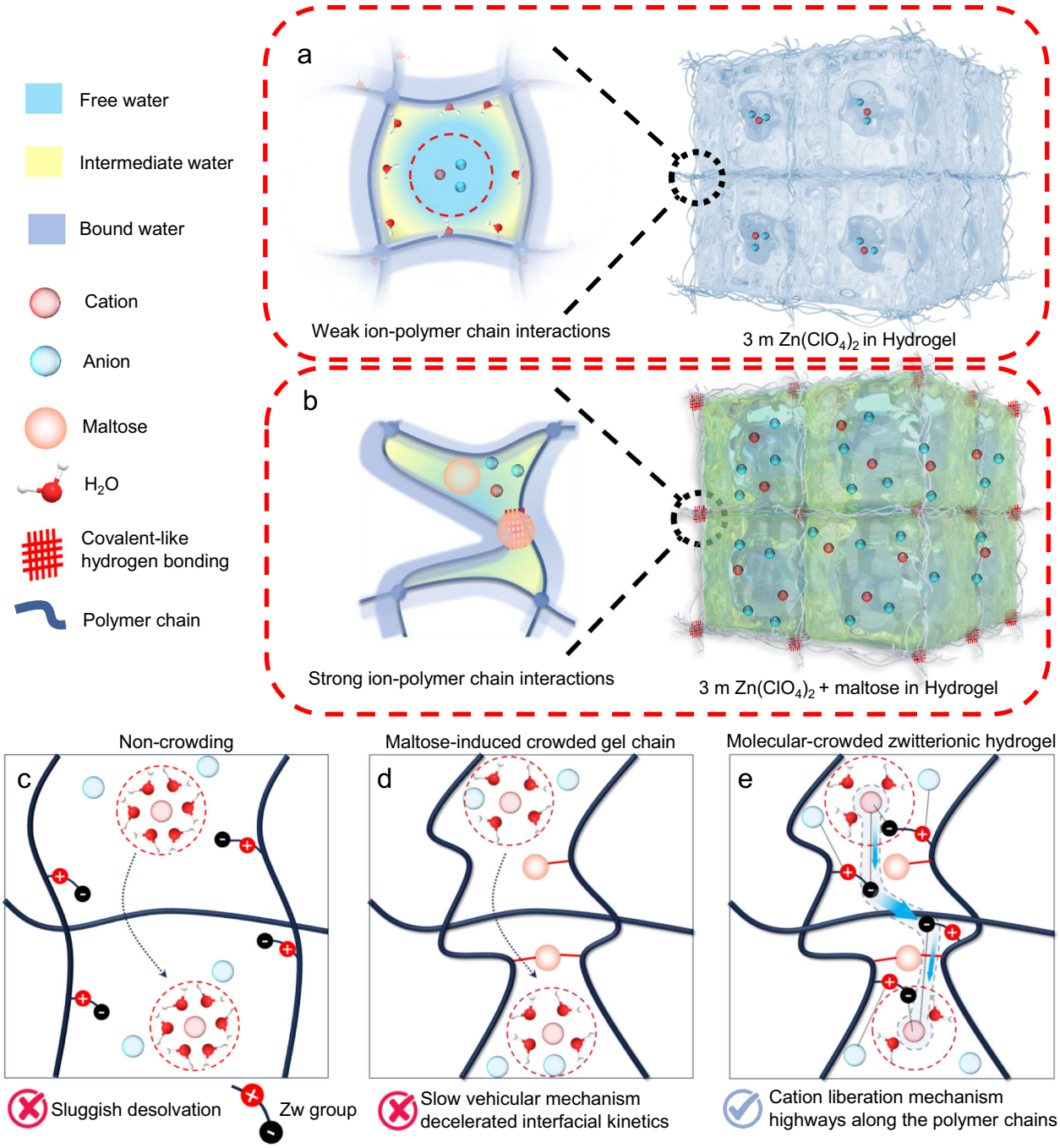

Fig. 1 | Schematics of the states of polymer chains with different electrolytes. **a** Weak interaction between ions and gel chains with dilute electrolytes. **b** Strong interaction between ions and gel chains by dual induction of maltose molecules. Schematic diagram of (**c**) Sluggish ion desolvation in non-crowding hydrogel electrolyte, and (**d**) confined ion transport in traditional molecular-crowded hydrogel electrolyte, and (**e**) the alternative highways along the polymer chains for ion transport in crowded zwitterionic gel electrolytes.

denoting that the bulk CIPs from the zinc salt are diminished as the anions are crowded toward the positively charged group on the Zw backbone[32].

Such coordination interactions are also directly corroborated by the ^{67}Zn nuclear magnetic resonance (NMR) spectroscopy. As shown in Fig. 2f, the maltose crowded $Zn(ClO_4)_2$ electrolyte shows a chemical shift of 0.58 ppm from the pristine bare $Zn(ClO_4)_2$ equivalent (− 0.52 ppm). This shift is possibly from the reduced shielding effect by more anions and/or less water molecules within the Zn^{2+} primary solvation shell, as a result of the crowding effect[33–36]. With the Zw matrix, the ^{67}Zn resonance peak further displays a chemical shift to downfield of 2.65 ppm, strongly insinuating the much more intense interaction between Zn^{2+} and the sulfonate group ($-SO_3^-$, which has better coordination capability and de-shielding effect than ClO_4^-) on the polymer backbone. Meanwhile, the gradually broadened resonance peak also highlights a substantially reduced Zn^{2+} exchange rate during the acquisition time that is caused by enhanced Zn^{2+}-sulfonate interaction[33,37]. Hence, as summarized in Fig. 2g, h, the maltose molecules of the original crowding electrolyte exert dual roles within the Zw hydrogel matrix, impacting both the gel framework and the ions. In detail, the polymer chains are drawn together through the covalent-like hydrogen bonds facilitated by maltose, creating a confined space[38]. This rearrangement bridges the otherwise separate charged polymeric chains (caused by the anti-polyelectrolyte effect of Zw hydrogels), which avails the

https://doi.org/10.1038/s41467-025-66041-y

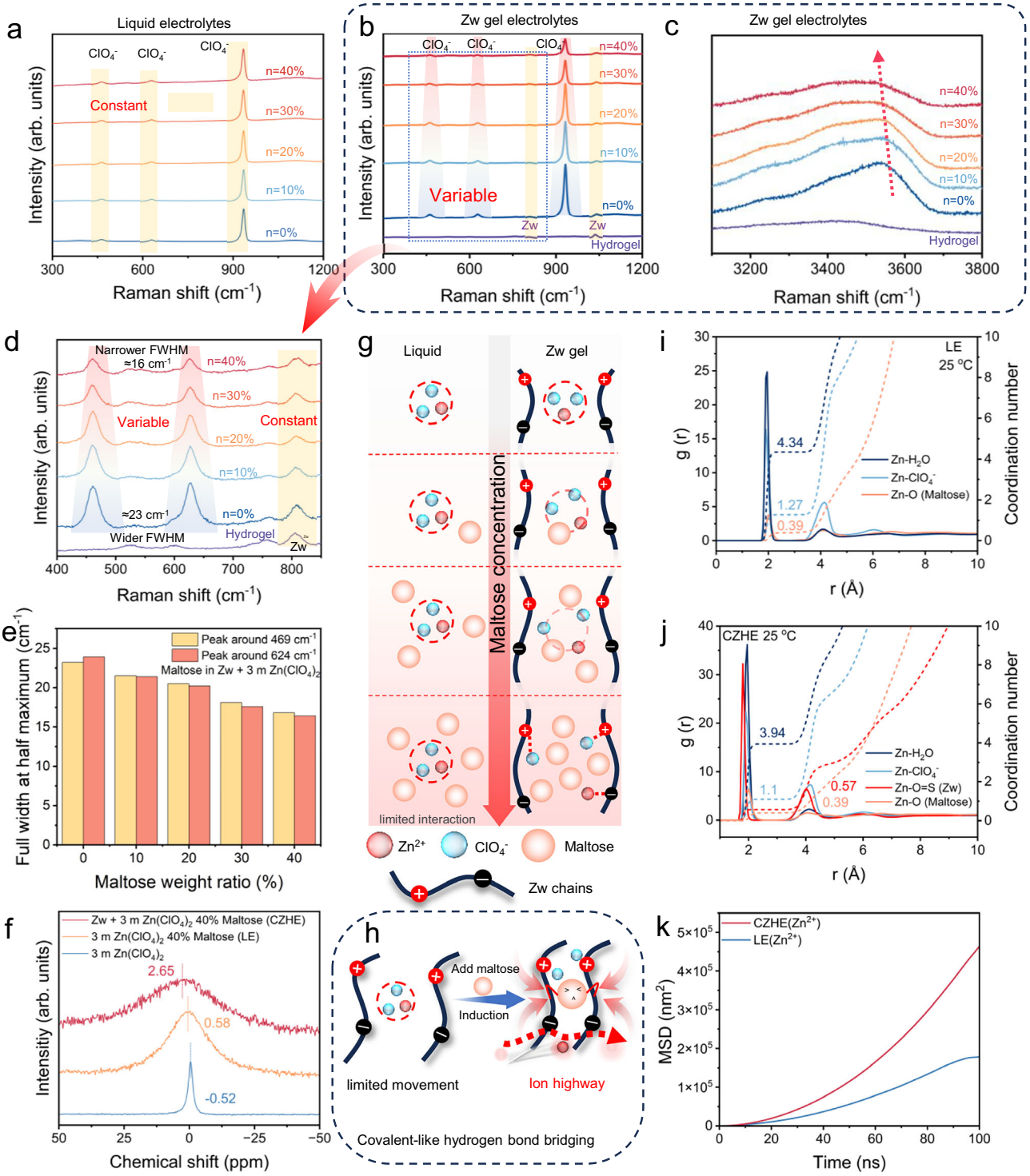

Fig. 2 | Study of enhanced ion-polymer interactions and promotion of Zn^{2+}. **a** Raman spectra of the liquid electrolytes (LEs) containing 3 m $Zn(ClO_4)_2$ with the varied maltose concentration gradients. **b**, **c** Raman spectra of the zwitterionic (Zw) HE containing 3 m $Zn(ClO_4)_2$ with varied maltose concentration gradients. **d** Enlarged Raman peaks of ClO_4^- solvation configurations, showing the variation in full width at half maximum (FWHM). **e** Variation of the FWHM values of the Raman peak corresponding to the ClO_4^- solvation configuration in serial 3 m $Zn(ClO_4)_2$ Zw gel electrolytes. **f** ^{67}Zn NMR spectra of different electrolytes. **g**, **h** Schematic diagram of the effect of maltose on gel chains and ions. Radial distribution functions and corresponding coordination plots of Zn^{2+} in **i** liquid electrolyte (LE) and **j** crowded Zw hydrogel electrolytes (CZHEs). **k** MSD plots of Zn^{2+} in LE and CZHE under electrical field at 25 °C.

polymer-ion interactions. Within this confined space, the crowded maltose molecules also push anions and cations to the intrinsically dissociated counterionic sites of "inner salt" chains, thereby effectively dissociating the possible CIPs induced by the crowding effect. However, it is worth mentioning that the 40 wt% maltose crowded Zw hydrogel electrolyte has a much lower free water content than that of the liquid equivalent (5.4% vs. 25.2%, Supplementary Figs. 1e, 2e). Given the advantages of reduced free water, hereinafter, CZHE and LE refer exclusively to the 40 wt% maltose-based gel electrolyte and liquid electrolyte, respectively.

To further uncover Zw matrix's impacts on ion speciation and coordination configurations in the crowded electrolyte, we performed molecular dynamics (MD) simulations on CZHE, LE, with bare 3 m $Zn(ClO_4)_2$ electrolyte as a reference (Fig. 2i–k, Supplementary Figs. 5–8, Supplementary Data 1). The snapshots in Supplementary Fig. 5 show that the ions and maltose are generally homogeneously distributed in the polymer and/or water matrix. The radial distribution functions (RDFs) and specific coordination numbers (CNs) show that, within LE, one Zn^{2+} ion is solvated with 4.34 H_2O, 1.27 ClO_4^-, and 0.39 maltose in its first solvation sheath (Fig. 2i). In contrast to the case in bare 3 m $Zn(ClO_4)_2$ electrolyte with or without Zw polymer (Supplementary Fig. 6 and 7), the maltose crowding agent can notably decrease the number of the cation's solvation H_2O (from 4.91 to 4.56 on average), though it has weak solvation capability. The reduced solvation water can potentially ameliorate side reactions and facilitate the desolvation process. Nonetheless, the crowding environment incurs an increased CN of ClO_4^- from 1.09 to 1.27 (Fig. 2i, Supplementary Fig. 6b), along with a substantially elevated CIP portion (18.9% to 42.5%, Supplementary Fig. 8a). More CIPs will impair the ionic conductivity of the electrolyte and cause capacity loss, particularly at low temperatures[39].

Upon introducing Zw polymer, the maltose coordination remains almost unchanged, but the negatively charged sulfonate group from the Zw backbone enters the primary solvation shell of Zn^{2+}. Remarkably, this cation-polymer interaction favors a reduced CN of H_2O and ClO_4^- to 3.94 and 1.1, respectively (Fig. 2j). The CIP also shows a dramatic decline from 42.5% to 24.4% (Supplementary Fig. 8). Note these values are very close to the experimental results from deconvoluted Raman spectra analysis (Supplementary Fig. 1b, 1f,1g, 2b, 2f, 2g, Table 1). Such evolution trends can be rationalized by the crowding effect of maltose on ions within CZHE, consistent with the above spectroscopic results (Fig. 2d–f). In other words, the gel matrix of CZHE can strengthen the crowding effect of expelling solvated water, yet circumvent its drawback of the inevitably induced CIPs, thereby ensuring prompt ion migration kinetics. As such, the dynamic behavior of Zn^{2+} in different electrolytes were compared by computing the mean square displacement (MSD) at 298.15 K (Fig. 2k). It can be ascertained from the MSD profiles that under an external electric field the migration capability of Zn^{2+} in CZHE considerably surpassed that in LE, validating that the enhanced polymer-ion interactions can effectively leverage the ion hopping channels along the Zw backbone cohort. Taken together, the MD simulation results coincide well with the Raman and NMR measurements, both suggesting that the maltose-induced reciprocal effort of ions and polymer chains can essentially confine free water, reduce solvated water and CIPs, and harness the elaborated ion transport highways.

Electrochemical performance and enhanced interfacial kinetics of CZHE

For an intuitive comparison of the facilitated Zn^{2+} migration in CZHE, its ionic conductivity was compared with that of LE. The influence of the gel backbone was additionally benchmarked with two other types of crowded HE, i.e., the neutral polyacrylamide (PAM) and a polyanion (poly zinc 2-acrylamido-2-methylpropanesulfonate, marked as PAMPS) electrolytes. All three HEs share the same acrylamide basal moiety except for the different charged groups (Supplementary Fig. 9), hence PAM and PAMPS can be ideal references to verify the role of the ion hopping channels in the Zw HE. Figure 3a shows the Arrhenius plot of the ionic conductivity of different electrolytes (all HEs containing 40 wt% of maltose crowded 3 m $Zn(ClO_4)_2$) as a function of temperature. The CZHE affords a much higher ionic conductivity and a lower activation energy (E_a) than the two control HEs, attesting the critical role of the zwitterion effect[21]. Further, unlike commonly observed decreased ionic conductivity when transforming LE to quasi-solid-state gel electrolytes, here the CZHE demonstrated even slightly better conductivity than that of LE. At 25 °C, the CZHE has a high ionic conductivity of 33.1 mS cm^{-1}, meeting the requirements of high-rate RZMBs. Within the low-temperature region (−60 – 0 °C), the CZHE also displays the lowest E_a of conductivity among all the electrolytes, indicating the Zn^{2+} migration barrier is reduced more prominently at low temperatures by the Zw gel matrix. As a result of the dramatically diminished free water over LE, the electrochemical stability window of CZHE is broadened from 2.1 to 2.6 V (Fig. 3b), enabling potential energy-dense Zn^{2+} storage. Moreover, the CZHE delivers a Zn^{2+} transference number ($t_{Zn^{2+}}$) up to 0.67, much higher than the LE of 0.24 (Fig. 3c, Supplementary Fig. 10). Such a drastic improvement can be synergistically attributed to the dehydration-enhanced anion-polymer interactions (Fig. 2d) that hinder ClO_4^- transport[40], and the elevated kinetics for more selective and prompt Zn^{2+} migration (Supplementary Fig. 11). Given the dual induction effect from maltose, the CZHE also features decent mechanical strength (Supplementary Fig. 12), enabling additional functions as a flexible electrolyte for emerging wearable electronics.

The influence of the electrolytes on the reversibility and stability of Zn negative electrode was then assessed. Figure 3d shows that the Zn||Zn symmetric cell assembled from the CZHE can strip and plate stably at 1 mA cm^{-2} and 1 mAh cm^{-2} for 1200 h, while the LE-based cell can only run for about 300 h before short-circuiting yet with a larger voltage loop gap. A parallel control cell assembled from the non-crowded Zw HE delivered an even shorter duration of less than 100 h (Supplementary Fig. 13). The significantly extended lifespan of the symmetric cells by CZHE is probably rendered by the effective confinement of free water, which prevents side reactions and dendrite formation during Zn plating/stripping. Such conclusions are also consolidated by the water-retention test, which shows the CZHE can tightly hold the water within 200 days (94% retention) in ambient environment (Supplementary Fig. 14). The CZHE can support the cell to work at other customized current densities and capacity densities (Fig. 3e), with a maximum Zn negative electrode depth of discharge (DOD) of 57%. For example, at a practical large rate of 3 mA cm^{-2} and 3 mAh cm^{-2}, the symmetric cell still sustained for 1000 h (Supplementary Fig. 15). Of particular note, in investigating the Zn plating/stripping stability of Zn||Zn symmetric cells, the suspected "soft short" may lead to a deceptive stability when operating cells at large current densities ($\geq$2 mA cm^{-2}). Here, we deployed the in situ temperature response test to scrutinize this issue. After the Zn plating/stripping at different rates (Fig. 3e), the symmetric battery displays increased voltage gaps at lower temperatures, yielding a positive E_a in the dynamic stripping/plating process (Fig. 3f, Supplementary Fig. 16). This positive E_a aligns with the characteristics of ionic conduction (the electronic conduction mechanism in short-circuit would result in a negative E_a), thereby confirming the genuinely stable interfacial reactions enabled by CZHE. The enhanced reversibility of the Zn interface by CZHE was also assessed with Zn||Ti asymmetric cells, which sustained well for 600 cycles with a high average coulombic efficiency (CE) of 99.6% (Fig. 3g, h), both substantially surpassing that of LE (Supplementary Fig. 17).

It is known that interfacial charge transfer is critical for the electrolyte-electrode stability, which even becomes the rate-determining step in electrochemical reactions under high current densities and/or low temperatures[41]. Besides, the divalent Zn^{2+} ion has intense interactions with its aqua and anion ligands, such that its sluggish desolvation process impedes the kinetics at the electrode-electrolyte interface and leads to aggravated battery polarization and diminished rate performance[42,43]. Hence, the desolvation kinetics of the cation in different electrolytes was studied in Zn||Zn symmetric cells by electrochemical impedance spectroscopy (EIS). Note that the interfacial processes are usually coupled/convoluted (e.g., adsorption, interfacial Zn^{2+} desolvation, and possible diffusion in passivation/interphase layers). To avoid the erroneous pre-modeling of the equivalent circuit model method that leads to possible

https://doi.org/10.1038/s41467-025-66041-y

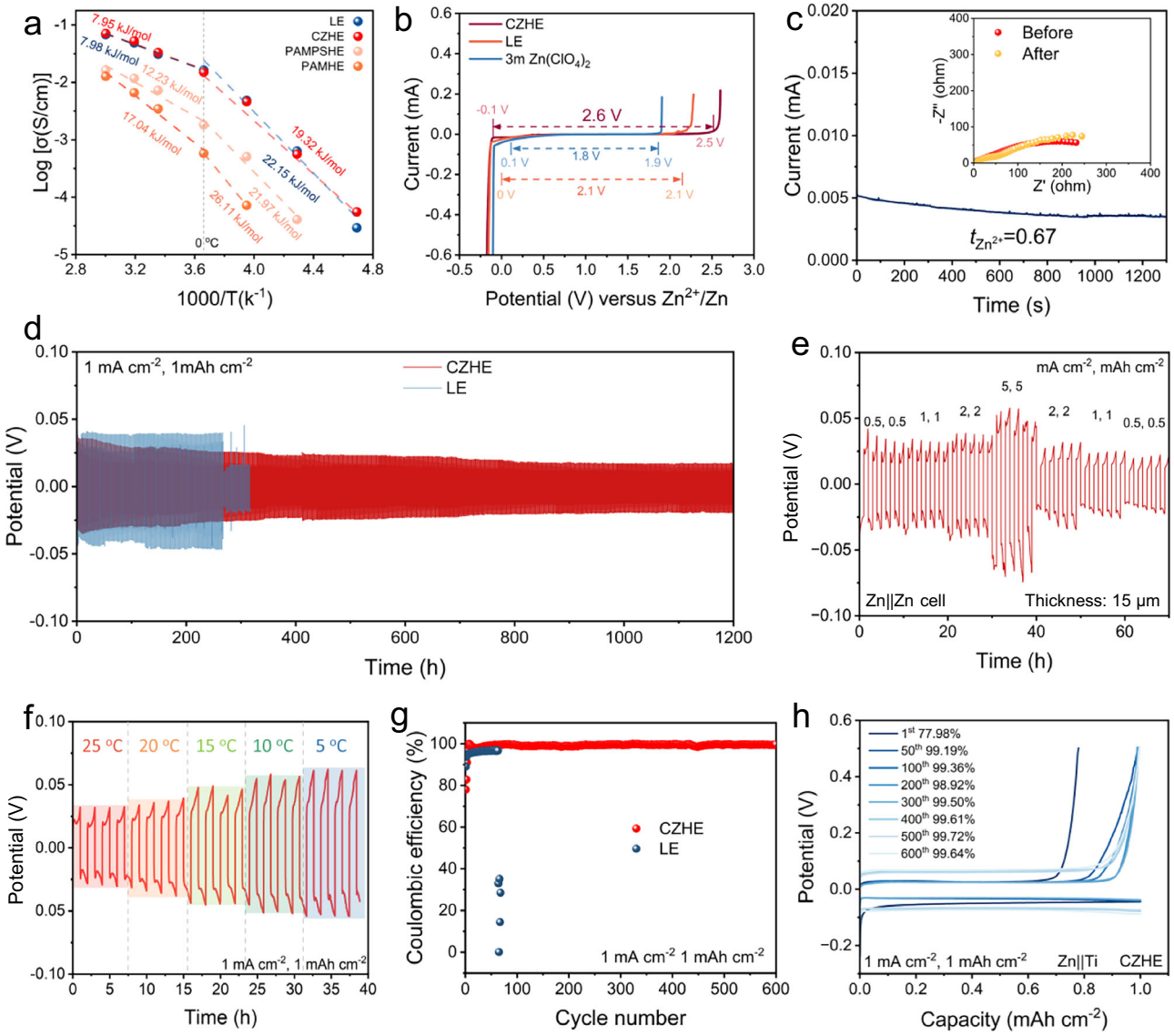

Fig. 3 | Electrochemical characterizations of electrolytes and negative electrode. a Plots of conductivity versus temperature for zwitterionic (Zw), poly zinc 2-acrylamido-2-methylpropanesulfonate (PAMPS), and polyacrylamide (PAM) soaked in 3 m $Zn(ClO_4)_2$ with 40 wt% maltose and liquid electrolyte (LE). **b** Electrochemical stability window of different electrolytes. **c** Direct current (DC) polarization curve of CZHE at 25 °C, inset shows electrochemical impedance spectroscopy plots before and after DC polarization. **d** Long Zn plating/stripping behavior and (**e**) Rate capability of symmetrical Zn | |Zn cells with different electrolytes. **f** Zn plating/stripping behavior under different temperatures after rate test. **g** Long-term cycle performance of Zn | |Ti asymmetric cells with different electrolytes at an upper cut-off voltage of 0.5 V. **h** Selected voltage-capacity profiles of Zn | |Ti with CZHE.

misunderstandings, the distribution of relaxation time (DRT) analysis that directly distinguishes the relaxation time (τ) constants of the principal electrochemical processes was used[44]. All the electrolytes show a temperature-dependent overall interfacial resistance (Supplementary Fig. 18). However, the deconvoluted charge transfer resistance (R_{ct}) of the CZHE-based cell is only about half of that of LE and bare 3 m $Zn(ClO_4)_2$ electrolyte based ones at all temperatures (Fig. 4a, b, Supplementary Fig. 19), denoting a much faster interfacial kinetics in the former. The E_a of interfacial desolvation process on CZHE-Zn interface is 21.81 kJ mol^{-1}, much smaller than the other two counterparts (Fig. 4c). This remarkably enhanced desolvation process is bestowed by the reduced solvated water and less ClO_4^- attraction in the Zn^{2+} solvation structure, as well as the selective hopping channel afforded by the Zw hydrogel matrix. Equally importantly, compared with LE, CZHE does not spawn the interfacial diffusion resistance (R_{dif}), which is most probably engendered by the passivation layer on the Zn negative electrode surface resulting from excess free water and more solvated water as discussed above. This trend was also validated by 3 m $Zn(ClO_4)_2$ electrolyte, where a much more significant R_{dif} is proliferated particularly at low temperatures (Supplementary Fig. 19). The boosted desolvation and the exemption of R_{dif} well account for the better rate performance and reversibility of CZHE over LE in different cells (Fig. 3d, g).

To assess the generality of this sugar crowding agent-induced interfacial regulation strategy, other hydroxyl-rich saccharides such as sucrose and fructose were also evaluated in the same CZHE framework. Despite structural differences from maltose, both sugar-based CZHEs exhibited comparable (or even better) ionic conductivity, remarkably suppressed passivation features, and reduced charge transfer resistances with regard to their respective liquid counterparts (Supplementary Figs. 20–22). Their interfacial desolvation activation energies were also significantly lower than those of LEs (Supplementary Fig. 23), indicating that the sugar-induced water immobilization and solvation modulation effects are broadly applicable, though the

https://doi.org/10.1038/s41467-025-66041-y

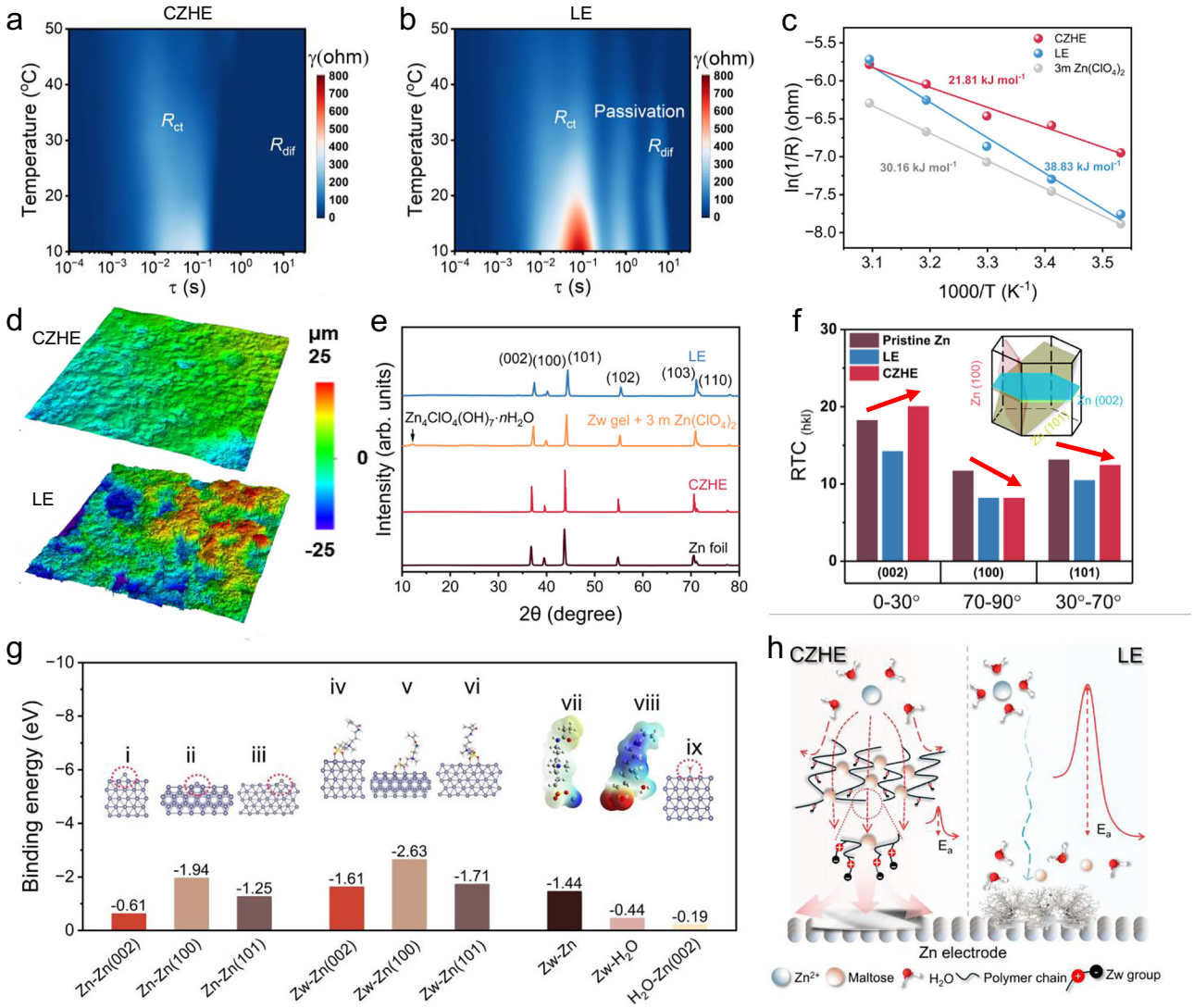

Fig. 4 | Material characterizations of the Zn electrode and the mechanism of (002) induced formation. **a** DRT contour plots of Zn^{2+} desolvation with CZHE (Rct. charge transfer resistance; R_{dif}: interfacial diffusion resistance). **b** DRT contour plots of Zn^{2+} desolvation with LE. **c** Corresponding activation energies derived by Arrhenius fitting. **d** 3D morphology images (size 258 × 258 μm) for Zn in the Zn | |Zn symmetric cells after cycling (50 cycles at 1 mA cm^{-2} and 1 mAh cm^{-2} and 25 °C) using CZHE and LE. **e** XRD patterns of bare Zn and post-cycled (after 50 cycles at 1 mA cm^{-2} and 1 mAh cm^{-2} and 25 °C) Zn with different electrolytes. **f** Relative texture coefficients ($RTC_{(hkl)}$) of pristine Zn and Zn cycled in different electrolytes. **g** Relaxed calculation models for Zn^{2+} and Zw monomer adsorption onto different planes along with corresponding adsorption energy values; the binding energies of Zw with Zn and water molecules, as well as the adsorption of H_2O onto the Zn (002) plane, are presented. (Atom color code: Zn, cyan; O, red; S, yellow; H, white; N, violet; C, gray.) **h** Schematic of desolvation and interfacial behaviors with different electrolytes.

extent of enhancement varies depending on the specific sugar-gel interactions.

The tuned interfacial reaction by CZHE is crucial for the regularity of Zn negative electrode surface. The 3D morphology scanning image shows that the post-cycled Zn surface is compact and dendrite-free, and combined XRD patterns verify that no byproducts (e.g., $Zn_xClO_4(OH)_y$) formed during the cycles (Fig. 4d, e). Also, after 20 cycles with CZHE, the electro-crystallization orientation (ECO) analysis of the Zn negative electrode based on the relative texture coefficient ($RTC_{(hkl)}$) shows an increased $RTC_{(002)}$ with declined $RTC_{(100)}$ and $RTC_{(101)}$ (Fig. 4f, Supplementary Fig. 24), highlighting the regulated Zn [002]-preferred deposition texture that contributes to the even surface[45,46]. In comparison, the cycled Zn negative electrode in LE exhibits comparatively random ECOs with significant irregular morphologies (Fig. 4d, Supplementary Fig. 25), which are probably caused by the passivation layer (Fig. 4b) and the low $t_{Zn^{2+}}$-resulted polarization (Supplementary Fig. 11). The effectiveness of the Zw gel backbone was further validated by the referenced non-crowded HE (Supplementary Fig. 26).

The underlying impact of the Zw gel matrix on the ECO was then evaluated by density functional theory (DFT) calculations (Fig. 4g, Supplementary Fig. 27, Supplementary Data 1). On the bare Zn surface, the interfacial Zn^{2+} will be preferably plated on (100) and (101) facets of the hexagonal close-packed Zn substrate, given their much higher binding energy (BE) with Zn^{2+} than that of the (002) facet (i-iii in Fig. 4g). Therefore, if not regulated, Zn^{2+} will continuously be plated along (100) and (101) and gradually induce the "tip-effect" sites, which are the main culprits of dendrite formation and/or side reactions[45]. However, with Zw matrix the high energy (100) and (101) planes can be efficiently blocked, as a result of the preferential adsorption of the polymer backbone on them (iv-vi in Fig. 4g). In this scenario, the natural deposition propensity of Zn atoms is guided along the (002), thereby rendering a more compact and stable Zn deposition texture. Further, the intense Zn-polymer interaction hinders the in-plane diffusion, and the hydration effect of the

https://doi.org/10.1038/s41467-025-66041-y

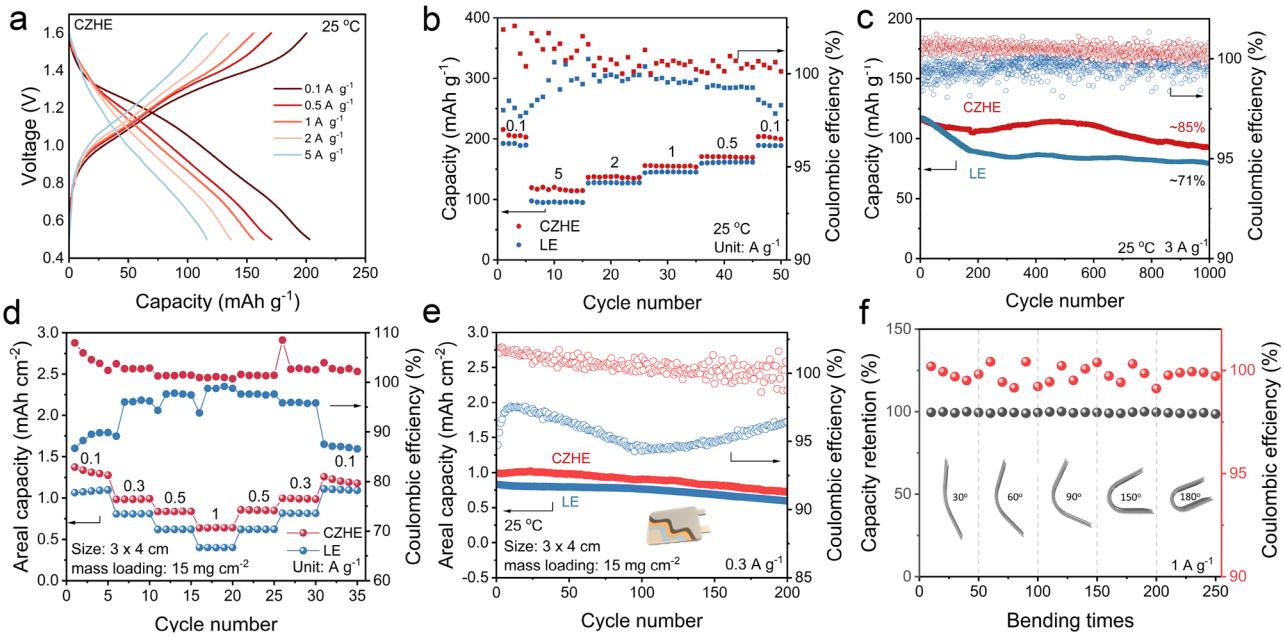

Fig. 5 | The performance of Zn | |PANI batteries at 25 °C. a GCD profiles of batteries with CZHE at various specific currents. Comparison of (**b**) the rate performances and (**c**) cycling performances at 3.0 A g^{-1} of batteries assembled with CZHE and LE. Comparison of (**d**) rate performance and (**e**) cycling performance of pouch cells with different electrolytes. **f** Electrochemical performance of the flexible RZMBs at 1 A g^{-1} with different bending angles.

Zw backbone also restricts the accessible free water on the otherwise bare water-Zn interface (vii-ix in Fig. 4g and Supplementary Fig. 28), both enabling a uniform Zn morphology with eliminated side reactions. In a nutshell, the incorporated Zw matrix fully leverages the advantages of molecular-crowding electrolytes while offering higher ion migration rates, larger $t_{Zn^{2+}}$, and improved interfacial kinetics (illustrated in Fig. 4h), fundamentally overcoming the critical issues associated with such electrolytes.

Electrochemical performance of full RZMBs and their low-temperature adaptability

The practical utilization of CZHE was evaluated in a full battery by pairing the polyaniline (PANI) positive electrode and Zn negative electrode alongside the electrolyte. Benefiting from the higher ionic conductivity and better interfacial kinetics, the CZHE based battery delivered obviously better rate capability than the LE-based equivalent (Fig. 5a, b, Supplementary Fig. 29). The reversibility of the Zn|CZHE | PANI battery was also high, as indicated by its higher CEs at different rates, particularly under low specific currents (Fig. 5b). After 1000 cycles at 3 A g^{-1}, the quasi-solid-state battery could deliver a reversible capacity of 92.6 mAh g^{-1} with a capacity retention of 85%, also surpassing that of the LE-based battery (Fig. 5c). Even after 4000 cycles at a high current density of 5 mA cm^{-2}, the quasi-solid-state battery retained 83.4% of its initial capacity (Supplementary Fig. 30), and the Zn surface in the CZHE remained relatively smooth and uniform (Supplementary Fig. 31). Meanwhile, compared with LE, the CZHE-based battery exhibits strong self-discharge resistance, retaining the highest voltage and 91.2% of its capacity after 24 h (Supplementary Fig. 32).

To meet realistic requirements of high areal capacity and large electrode areas, a pouch cell was assembled. The pouch cell utilizes a PANI loading mass of 15 mg cm^{-2} and a polished Zn foil of 15 μm thickness (with a negative electrode-to-positive electrode (N/P) mass ratio of 0.71:1) over an area of 12 cm^2 (3 × 4 cm). The thus assembled pouch cell featured a maximum areal capacity of 1.3 mAh cm^{-2} at a practical low rate of 1.15 C (Fig. 5d). It also delivered an average areal capacity of about 1 mAh cm^{-2} and higher CE for 200 charge-discharge cycles at 0.3 A g^{-1} (Fig. 5e). To further validate the practical relevance of CZHE for high Zn utilization, we assembled Zn||NaV_3O_8·1.5H_2O (NaVO) full batteries using a thin 10 μm Zn negative electrode (Supplementary Fig. 33). The CZHE-based pouch cell delivered a peak areal capacity of 3.2 mAh cm^{-2}, corresponding to a Zn depth of discharge (DOD) of 55%. CZHE enabled such pouch cells to retain 82.6% capacity after 350 cycles, which is higher than that of the LE-based counterpart (Supplementary Fig. 33d). Post-Zn plating/stripping scanning electron microscopy (SEM, Supplementary Fig. 34) checking the negative electrode further confirms the smoother Zn surface, indicating effective dendrite suppression and stable Zn plating/stripping enabled by CZHE.

Inherited from the flexible nature of CZHE, a flexible RZMB (with a device thickness of 0.67 mm, Supplementary Fig. 35) can be fabricated, which sustained stable performance despite different bending angles across 250 times of deformation (Fig. 5f). The flexible batteries could be connected in tandem for customized applications, as exemplified by powering a typical light-emitting diode belt upon bending (Supplementary Fig. 35 d).

The more favorable ion conduction and desolvation process of CZHE over LE was more clearly demonstrated in Zn-ion hybrid capacitors (ZIHCs)[47,48]. CZHE enabled ZIHCs to deliver a high specific energy of 186.7 Wh kg^{-1} at a specific power of 11 kW kg^{-1} (based on the active positive electrode material) and a maximum areal capacity of 1.41 mAh cm^{-2} at 1 A g^{-1} (Supplementary Figs. 36–39), representing decent performance among ZIHCs based on different gel electrolytes[14]. The CZHE additionally endowed strong anti-self-discharge capability (83.7% capacity retention after 120 h, Supplementary Fig. 40), enabled by the crowded and coordinated configurations that inhibit the self-diffusion of the adsorbed ions.

A vital challenge for concentrated and crowded electrolytes is their severely deteriorated performance at subzero temperatures, given the high viscosity and sluggish kinetics of these electrolytes become key barriers for battery operations[9,49]. Differential scanning calorimeter (DSC) tests revealed the CZHE possesses a solid-liquid transition temperature (T_t) down to −90 °C, much lower than that of the LE and bare 3 m $Zn(ClO_4)_2$ electrolyte (Fig. 6a). Such a lowered T_t is reasonably warranted by the combined hydration effect and ion-dipole interactions in CZHE that deconstruct the tetrahedral hydrogen bonding network of water and deter ice crystallization and salt precipitation. MD simulations were also performed to check the

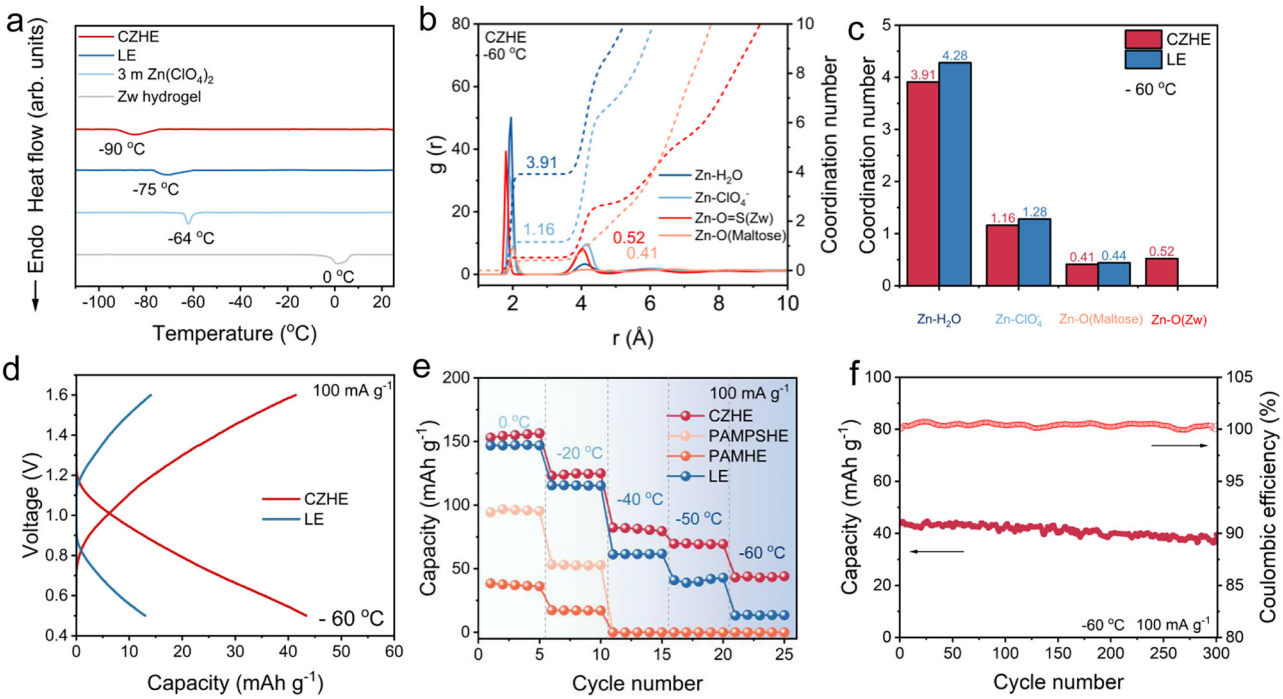

Fig. 6 | Properties of electrolytes and battery performance at low temperatures. a Differential scanning calorimetric thermograms of electrolytes recorded at 5 °C min^{-1}. **b** Radial distribution functions and corresponding coordination plots of Zn^{2+} in CZHE at −60 °C. **c** Comparison of Zn^{2+} solvation structures in CZHE and LE at −60 °C. **d** GCD curves of Zn | |PANI batteries with different electrolytes at −60 °C. **e** The temperature-dependent performances of batteries using different gel electrolytes. **f** Cycling performance of batteries with CZHE at 3.0 A g^{-1} under −60 °C.

temperature-dependent solvation configuration of the electrolytes. When the temperature varied from 25 to −60 °C, noticeable changes include the increased CN of maltose (0.39 to 0.41) in the first solvation sheath of Zn^{2+} accompanied by the reduced number of solvated water (3.94 to 3.91) in CZHE (Figs. 2j, 6b, Supplementary Data 1). Moreover, the cation-anion interaction was strengthened at low temperature, as evidenced by more CIPs (27.8%) over the 25 °C equivalent (24.4%, Supplementary Fig. 8). Despite so, compared with the coordination configurations in LE, CZHE features obviously less solvated water (4.28 vs. 3.91) and CIPs (46.7% vs. 27.8%), as a result of the intense cation-polymer (i.e., Zn^{2+}-sulfonate on Zw backbone) interactions at −60 °C (Fig. 6c, Supplementary Fig. 8, 41b). The optimal ion speciation and their migration kinetics therefore elucidate the higher ionic conductivity as well as the better interfacial kinetics in CZHE at lower temperatures measured above (Figs. 3a, 4c). As a result, the CZHE-based Zn | |PANI battery delivered a specific capacity of 44 mAh g^{-1} at 0.1 A g^{-1} under −60 °C, higher than that of the LE-based batteries (Fig. 6d). The zwitterionic effect was essential for the low-temperature performance of CZHE, as compared with the other two crowded HEs (Fig. 6e). The Zn|CZHE | PANI could run stably for 300 cycles with a CE of 100% (Fig. 6f), suggesting its good low-temperature adaptability.

General applicability

To further verify the practical relevance of the sugar-induced crowding strategy, full-cell evaluations were carried out using sucrose-based and fructose-based CZHEs in Zn | |PANI configurations. Both systems delivered higher capacities and improved CEs across a range of specific currents compared to their respective LE counterparts (Supplementary Fig. 42), affirming that the conductivity and interfacial kinetic advantages imparted by sugar-induced water-ion regulation can be translated into enhanced device-level performances. These results reinforce the general applicability of the strategy, although the degree of improvement depends on the specific molecular characteristics of the sugar used.

More critically, in light of the successful demonstration of the crowding induced ion-liberation effect in Zw gel matrix, we envisage it is universal to various aqueous mono- or multi-valent ion chemistries (as illustrated in Fig. 7a). Therefore, the general applicability of the CZHE in mono- or multi-valent batteries was further demonstrated by rechargeable Na^+ ion batteries (NIBs) and Mg^{2+} ion batteries (MIBs) with different anion-based salts. The CZHE and LE were prepared by adjusting 40 wt% maltose in 3 m NaCl or 3 m $Mg(NO_3)_2$ aqueous electrolyte for the two batteries accordingly. PANI and commercial activated carbon (AC) were used as the positive electrode and negative electrode material in both batteries to exclude the possible disturbance from different electrode materials. As expected, the different CZHEs again exhibited an ionic conductivity almost identical to their LE equivalents (Supplementary Fig. 43). When used in the two batteries, the CZHE-based batteries delivered obviously better rate capability compared with those assembled with LE (Fig. 7b, d), presumably because of the facilitated interfacial desolvation kinetics by CZHE. The trend is more prominent in MIBs, since Mg^{2+} has a higher charge density and stronger solvation interactions with water, which entails more desolvation penalty than that of Na^+[50,51]. This in turn corroborates the fact that CZHE indeed enables fast desolvation kinetics and is particularly beneficial for high-rate multivalent ion batteries. Moreover, both the MIB and NIB based on the CZHE afforded satisfactory stability during cycling, also with better reversibility than their LE counterparts (Fig. 7c, e). These results prove the ion-liberation effect of CZHE can be harnessed in various aqueous batteries.

Discussion

In summary, we demonstrated a molecular crowded Zw HE that can leverage the advantages of molecular crowding electrolytes while overcoming their critical associated issues. This was realized by the synergy of maltose's crowding effect and the Zw hydrogel matrix that regulated the ion-water-polymer interactions. As a result, the Zn^{2+} solvation structure was optimized with less solvated water and fewer

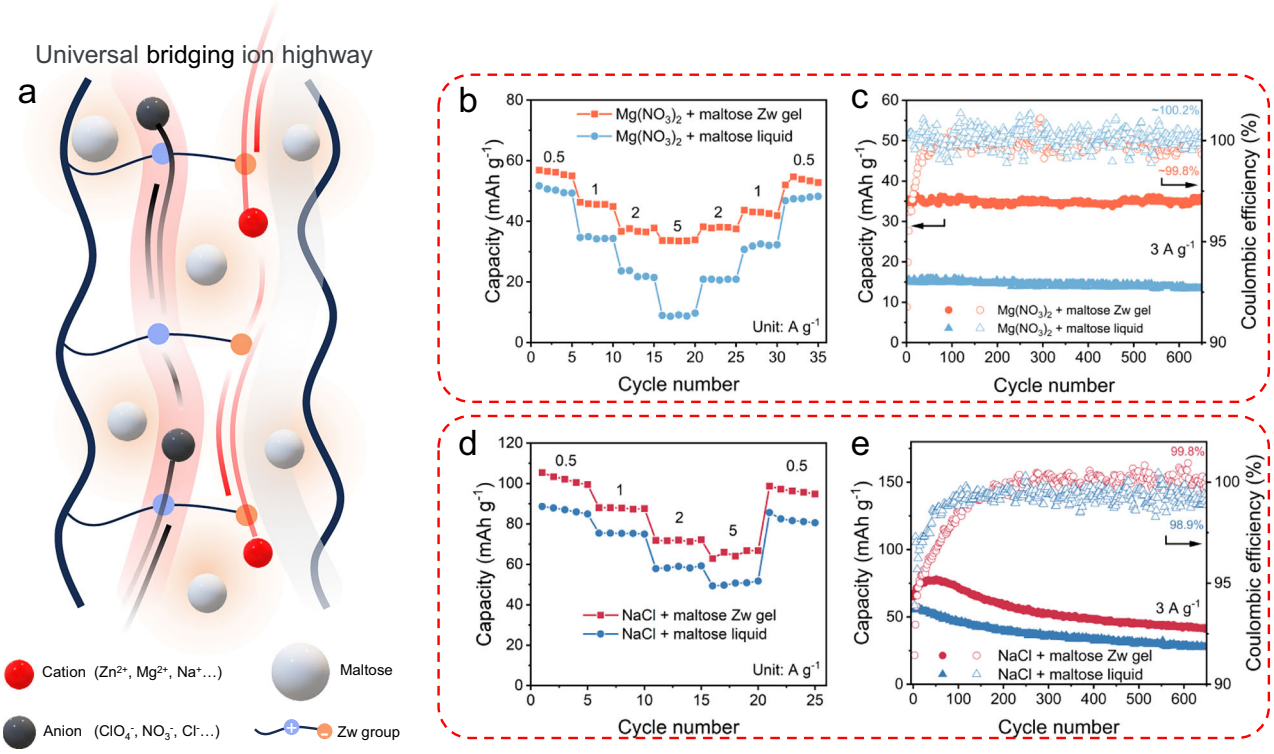

Fig. 7 | The electrochemical performances of the as-assembled AC || PANI for MIBs and NIBs. a Schematic diagram of the universality of maltose-bridged gel chains as ion highways. **b** Rate performance of MIBs at various specific currents with different electrolytes. **c** Cycling performance of MIBs with different electrolytes. **d** Rate performance of NIBs at various specific currents with different electrolytes. **e** Cycling performance of NIBs with different electrolytes.

CIPs, and the thus liberated Zn^{2+} can migrate more efficiently along the Zw polymer ion channel and desolvate effectively for subsequent interfacial reactions. The CZHE delivered an ionic conductivity comparable to or higher than that of liquid equivalents, yet with a wider electrochemical window of 2.6 V, a larger t_{Zn}^{2+} of 0.67, and facilitated desolvation kinetics. It also rendered stable and more regular Zn negative electrode interface at high utilizations (up to 55%) in high-areal capacity (> 3 mAh cm^{-2}) pouch cells. RZMBs and ZIHCs assembled with this CZHE afforded high stability, good rate capability, and adaptability to frozen temperatures (down to −60 °C). The general applicability of this CZHE can also be extended to aqueous Mg^{2+} and Na^{+} batteries, both surpassing their liquid counterparts. The results of this work are expected to open new avenues for the development of advanced electrolytes for sustainable energy storage.

Methods

Synthesis of the Zw Hydrogels

Zwitterionic (Zw) hydrogels were prepared by dissolving 20 g [3-(Methacryloylamino)propyl]dimethyl(3-sulfopropyl)ammonium hydroxide inner salt (≥ 97%, Sigma-Aldrich) monomer in 20 mL of deionized (DI) water under magnetic stirring for 10 min. Then, 7 mg N, N′-methylenebisacrylamide (BIS, ≥99.5%, Sigma-Aldrich) was introduced as a crosslinking agent, and the solution was stirred for an additional 30 min. 110 mg Ammonium persulfate, (APS, ≥98%, Sigma-Aldrich) was then added as an initiator. The mixture was then stirred continuously and bubbled with N_2 gas to remove O_2 at 0 °C for 0.5 h. Afterward, the above mixture was injected into a plastic mold and kept at 75 °C for 2 h to form Zw hydrogel.

Synthesis of the PAMPS Hydrogels

Poly sodium 2-acrylamido-2-methylpropanesulfonic acid (PAMPS) hydrogels were prepared by dissolving 20.7 g 2-acrylamido-2-methylpropanesulfonic acid (≥ 98.5%, Sigma-Aldrich) monomer in DI water (15 mL). A 5 mL aliquot of 20 M NaOH (prepared by NaOH pellets, ≥98%) was slowly added to adjust the solution to pH 7, followed by continuous stirring for 10 min to ensure uniform neutralization. Subsequently, 7 mg BIS was introduced as a crosslinking agent, and the mixture was stirred for another 30 min. 110 mg APS was then added as the initiator. The resulting precursor solution was then stirred continuously and bubbled with N_2 gas to remove O_2 at 0 °C for 0.5 h. Afterward, the above mixture was injected into a plastic mold and kept at 65 °C for 2 h to form PAMPS hydrogel.

Synthesis of the PAM Hydrogels

Polyacrylamide (PAM) hydrogels were prepared by dissolving 7 g acrylamide (≥ 99%, Sigma-Aldrich) monomer in DI water (22 mL) under stirring for 10 min. Then, 7 mg BIS was added into the solution as a crosslinker. After stirring for 30 min, 110 mg APS was added to the mixture as an initiator. The mixture was then stirred continuously and bubbled with N_2 gas to remove O_2 at 0 °C for 0.5 h. Afterward, the above mixture was injected into a plastic mold and kept at 65 °C for 2 h to form PAM hydrogel.

Preparation of PANI Electrodes

The polyaniline (PANI) was synthesized by APS oxidizing aniline monomer in HCl solution. Typically, 0.365 mL aniline (≥ 99.5%, Sigma-Aldrich) was added into 15 mL 1 M HCl (Sigma-Aldrich) in an ice bath under stirring for 1 h. 0.228 g APS was added into 5 mL 1 M HCl and was dropped into the above solution. After string for 1 h, the dark green sample was obtained. Then, sample was washed with DI water and ethanol and dried at 60 °C for 12 h. PANI positive electrodes were prepared by mixing PANI, carbon black (Super P, ≥99%, Alfa Aesar), and poly vinylidene fluoride (PVDF) binder (average M_w ~ 534,000 by GPC, Sigma-Aldrich) at a mass ratio of 7:2:1 in 1-Methyl-2-pyrrolidone (NMP, ≥99%, Sigma-Aldrich) solvent. The prepared slurry was uniformly coated onto carbon cloth (CeTech) using a doctor-blade

technique and subsequently dried in a vacuum oven at 60 °C overnight. The average electrode material loading on the carbon cloth was controlled at 1 ± 0.05 mg cm^{-2} for unit cells. For pouch cells, the loading mass of PANI was 15 ± 0.2 mg cm^{-2}.

Preparation of activated carbon electrodes

Activated carbon (AC) positive electrodes were prepared by mixing commercially available AC (YP-80F, Kuraray), carbon black, and PVDF binder at a mass ratio of 8:1:1 in NMP solvent. The mixture was then coated on to a carbon cloth (CeTech) by a doctor-blade and dried overnight in a vacuum oven at 60 °C. The average mass loading electrode materials on carbon cloth were 1, 2, 3, 5, 10 ± 0.1 mg cm^{-2}.

Preparation of $NaV_3O_8{\cdot}1.5H_2O$ Electrodes

The preparation method for $NaV_3O_8{\cdot}1.5H_2O$ (NaVO) involves adding 3 g of V_2O_5 powder (≥ 99%, Sigma-Aldrich) to 100 mL of a 2 M NaCl (prepared by NaCl powder, ≥99%, Sigma-Aldrich) solution, followed by magnetic stirring at 400 rpm for 72 h. The resulting orange-colored powders were then centrifuged and washed five times with deionized water and ethanol, and subsequently dried at 80 °C for 10 h. NaVO positive electrodes were prepared by mixing NaVO, carbon black, and PVDF binder at a mass ratio of 7:2:1 in NMP solvent. The mixture was then coated on to a carbon cloth by a doctor-blade and dried overnight in a vacuum oven at 60 °C. The average mass loading electrode materials on carbon cloth were 16 ± 0.2 mg cm^{-2} for pouch cells.

Assembly of flexible RZMBs and ZIHCs

The prepared Zw, PAMPS, and PAM hydrogels were soaked in 3 m $Zn(ClO_4)_2$ (prepared by $Zn(ClO_4)_2.6H_2O$, Sigma-Aldrich, where m denotes the molality, 1 m means 1 mol solute dissolved in per kilogram of DI water) and 3 m $Zn(ClO_4)_2$ with 40 wt% Maltose (≥ 95%, Sigma-Aldrich) solution for 72 h until they reached an equilibrated state. The hydrogels were then wiped-dried with lab tissues until there was no noticeable surficial liquid and carefully sliced to serve as gel electrolytes. Zn-metal battery unit cells (1 × 1 cm) were assembled by sandwiching hydrogel electrolytes (with a thickness of ca. 300 μm) between a Zn foil (contact area with HE of 1 cm^2) and a PANI-loaded carbon cloth (contact area 1 cm^2). ZIHC unit cells (1 × 1 cm) were assembled in the same way. In the case of liquid electrolytes, glass fiber filters were used as separators. The electrodes were manually cut to size using a high-precision stainless-steel guillotine cutter. The Zn foil in all the unit cells has a thickness of 50 μm (≥ 99.9%, Sigma-Aldrich). CR2032-type coin cells were assembled using stainless-steel cases and springs. Each cell contained a single-side coated positive electrode and a Zn electrode with 100 μL liquid electrolyte. For pouch cells, a sandwich structure was formed by stacking one positive electrode, the gel electrolyte, and one thin Zn (15 or 10 μm, ≥99.9%, Sigma-Aldrich) negative electrode. The assembled stack (3 × 4 cm effective area) was then enclosed in an aluminum-laminated pouch for sealing. Then, the pouch cells were degassed, heat-sealed, and cycled without additional external pressure. Zn foil was polished with sandpaper, rinsed with deionized water and ethanol, and dried in air before use.

Electrochemical measurements

Cyclic voltammogram (CV), galvanostatic charging/discharging (GCD), and electrochemical impedance spectroscopy (EIS) tests were performed by an electrochemical workstation (CHI 760E). EIS measurements were performed using a potentiostatic mode with an AC amplitude of 10 mV over the frequency range of 100 kHz to 0.01 Hz, with 12 points per decade. The cells were stabilized for 30 min at open-circuit voltage before each measurement. The electrochemical windows of the electrolytes were measured using an inert current collector (Ti foil, ≥99.99%, Sigma-Aldrich). Linear sweep voltammetry (LSV) measurements were carried out in a three-electrode configuration, where a titanium foil served as the working electrode, and two zinc foils were used as the reference and counter electrodes, respectively. The potential was scanned at a rate of 2 mV s^{-1} to evaluate the electrochemical stability of the electrolytes. Zn | |PANI cells were tested at voltage range of 0.5–1.6 V at 0.1, 0.3, 0.5, 1, 2, 3, 5 A g^{-1} Zn | |NaVO cells were tested at voltage range of 0.2–1.6 V at 0.1, 0.5, 0.6, 1, 2, 5 A g^{-1}. Zn | |AC cells were tested at voltage range of 0–2.2 V at 2, 5, 10, 20, 50, 100, 200 mV s^{-1} and 0.5, 1, 2, 5, 10 A g^{-1}. Zn | |Ti cells were pre-cycled at 1 mA cm^{-2} with a cutoff capacity of 1 mAh cm^{-2}. All the general electrochemical tests (CV, GCD, EIS, LSV) were performed in an open environment within a temperature range of 25 ± 2 °C. Long-term stability tests were conducted by a battery testing system (LANHE). For Zn | |Zn and Zn | |Ti cell tests, Zn foils of 15 μm or 50 μm were used. All the electrochemical energy storage tests and cycling experiments were conducted in an environmental chamber at a constant temperature of 25 ± 0.5 °C unless otherwise specified. The low-temperature performance was tested in a temperature chamber (−60-25 ± 0.5 °C).

For the calculation of specific capacity, specific current, and specific energy, the mass of the active material in the positive electrode was used as the reference. The specific capacity (C, mAh g^{-1}) was determined from the GCD profiles according to the following equation:

$$C = \frac{It}{3.6m} \tag{1}$$

where I (A g^{-1}) denotes the current density, t (s) is the discharge time, and m (g) represents the mass of the active material in the positive electrode.

The areal capacity (C_{areal}, mAh cm^{-2}) was calculated as the product of the specific capacity (C, mAh g^{-1}) and the active material loading ($m_{loading}$, g cm^{-2}) by the following equation:

$$C_{areal} = C \times m_{loading} \tag{2}$$

The capacity retention was calculated based on the discharge capacity of the first cycle as a reference.

The specific energy E and the specific power P of assembled ZIHCs were calculated from the following equations:

$$E = \frac{1}{2} C \times V \tag{3}$$

$$P = \frac{E}{t} \tag{4}$$

Physicochemical characterizations

The morphology and microstructure of as-prepared materials (cycled Zn) were examined by a research grade laser confocal microscope (Optical Olympus LEXT OLS5000) and a scanning electron microscopy (SEM, ULTRA Plus, Zeiss) were performed at an accelerating voltage of 5 kV. A PANalytical X'Pert Powder X-ray diffractometer (XRD) analyzed the crystal structure of samples with Cu K_α radiation (λ = 0.15418 nm) operating at 45 kV and 40 mA over a 2θ range of 10–80°, with a step size of 0.02° and a scan rate of 5° min^{-1}. After electrochemical cycling, the Zn electrodes were disassembled from the cells, rinsed with deionized water to remove residual electrolyte, and dried under vacuum at 25 ± 1 °C before ex situ characterization. Raman spectra were recorded using a Renishaw Raman inVia Reflex system under a 532 nm excitation laser at a power of 10 mW. The attenuated total reflection Fourier-transform infrared (ATR-FTIR) spectra were recorded on a Perkin-Elmer spectrometer in the transmittance mode with 32 scans at a resolution of 4 cm^{-1} and a scan rate of 2 cm^{-1} s^{-1}. ^{67}Zn nuclear magnetic resonance (NMR) spectra were collected with a Bruker AVIII 500 MHz NMR spectrometer, and 3 m $Zn(ClO_4)_2$ liquid

electrolyte was used as a reference for the ^{67}Zn NMR characterizations. The hydrogel polyelectrolytes' mechanical tests were conducted at 25 ± 1 °C using a universal mechanical tester (SUNS, Shenzhen, China). Rectangular hydrogel samples (30 × 10 × 0.3 mm) were clamped between grips and stretched at a constant strain rate of 10 mm min^{-1} until fracture. The stress–strain curves were automatically recorded to evaluate the tensile strength and elongation at break. The freezing and melting temperature of hydrogels was determined as the temperature where the melting ended using a differential scanning calorimeter (DSC) (Mettler Toledo 823e) at a scan rate of 5 °C min^{-1}, with the samples kept in a Pt pan.

Computational methods

All the spin theoretical DFT calculations were performed using the Vienna ab initio Simulation Package (VASP, version 5.4.4)[52,53]. The electronic exchange–correlation interactions were treated within the generalized gradient approximation (GGA) using the Perdew–Burke– Perdew–Burke–Emzerhof (PBE)[54]. The projector augmented-wave (PAW) methods[55,56] was applied to describe the interactions between core and electron (valence electron). A plane-wave basis set with a kinetic energy cutoff of 600 eV was employed. The ground-state structures were relaxed until the atomic forces on all atoms were smaller than 0.01 eV Å^{-1}, and the energy convergence criterion was defined as 1.0 × 10^{-6} eV per cell. The slab models of Zn (002), (100) and (101) surfaces were used with a 25 Å vacuum layer separation in z-direction. The (4 × 4) Zn (002) surface, (5 × 3) Zn (100) surface (3 × 3) Zn (101) surface were used to study the adsorption of Zn and Zwitterion on the surfaces using slab method. A surface-bulk like configuration was used by allowing the top three atomic layers to relax, while freezing the rest of atomic layers in their bulk coordinates. The Brillouin zone was sampled using a Monkhorst-Pack meshes with 5 × 5 × 1 (Supplementary Fig. 44 and Supplementary Table 2). The van der Waal (vdW) interactions are included by using DFT-D3 method of Grimme[57,58]. The adsorption energy was calculated using the following equation.

$$E_{ads} = E_{Zn+mol} - E_{Zn} - E_{mol} \tag{5}$$

where E_{Zn+mol}, E_{Zn} and E_{mol} are total electronic energies of Zn surface with adsorbed molecules, clean Zn surface and adsorbed molecule (including zwitterionic molecule, Zn atom and water molecule).

All molecular dynamics (MD) simulations were performed using an open-access GROMACS software package with the GAFF2 force field[59]. In this study, there are three models studied considering the presence of zwitterionic (Zw) hydrogel (poly[(3-(methacryloylamino) propyl)dimethyl(3-sulfopropyl)ammonium hydroxide] with 4 repeated units) and maltose as the additives. The simulation box size of 5 × 5 × 5 nm^3 was used as the initial box in all simulation models. First, a model of 3 m $Zn(ClO_4)_2$ consists of 150 $Zn(ClO_4)_2$ and 2778 H_2O molecules. Second, 3 m $Zn(ClO_4)_2$ 40 wt% maltose with Zw hydrogel electrolyte consists of 90 $Zn(ClO_4)_2$, 1667 H_2O, 59 maltose and 26 Zw polymer molecules. Third, 3 m $Zn(ClO_4)_2$ 40% maltose consists of 90 $Zn(ClO_4)_2$, 1667 H_2O and 59 maltose molecules. Fourth, 3 m $Zn(ClO_4)_2$ with Zw hydrogel electrolyte consists of 90 $Zn(ClO_4)_2$, 1667 H_2O and 26 Zw polymer molecules.

At the beginning of the simulation, structure and energy minimization of the systems were conducted. The ACPYPE was employed to obtain the GAFF2 force field topology[60]. The system was initially relaxed in the NVT ensemble at 298.15 K for 10 ns after the steepest descent minimization. Then it was annealed between 298.15 and 500 K for 5 ns, between 500 and 400 K for 5 ns, and between 400 and 298.15 K for 5 ns using the NPT ensemble (illustrated in Supplementary Fig. 45), with temperature and pressure coupling achieved through the Nose–Hoover and Parrinello–Rahman methods[61–64]. Additional annealing using NPT ensemble was also conducted for 10 ns at 213.15 K. The pressure was maintained at 1 bar. The electrostatic interactions were computed using PME methods. The final production simulations were performed under the NVT ensemble at 298.15 or 213.15 K for 100 ns. Electrostatic interactions in reciprocal space were calculated using a fast Fourier transform (FFT) grid spacing of 0.1 nm with cubic interpolation for charge assignment. Both electrostatic and van der Waals interactions were truncated at a cut-off distance of 1.2 nm. The Velocity Verlet integrator was employed with a time step of 1 fs. The cut-off distance of 1.2 nm was adopted for electrostatics and Van der Waals interactions. The Velocity Verlet integrator was adopted with a time step of 1 fs. The solvation structures analysis, including the distribution of contact ion pairs (CIP) and solvent-separated ion pairs (SSIP), and the radial distribution function and coordination number analysis, were performed using the trajectory from the last 80 ns out of 100 ns simulation time. The definition of the Zn^{2+}-anion coordination structures is illustrated in Supplementary Fig. 46. The salt–solvent clusters (SSIP, CIP, and AGG) are categorized based on the Zn^{2+}-anion CN obtained from MD simulations. In our CN analysis, Zn^{2+} and ClO_4^- are considered coordinated when the Zn^{2+} ion lies within 2.3 Å of any oxygen atom of ClO_4^-. This cutoff distance was derived from the Zn–O(ClO_4^-) RDF, where 2.3 Å corresponds to the first minimum following the primary peak, representing the boundary of the first coordination shell (as shown in Figs. 2i, 2j, 6b, and Supplementary Figs. 6, 7, and 41). Trajectories were analyzed by MDAnalysis code whenever the respective tool was unavailable in GROMACS[65,66].

To further investigate the influence of electric field on the drift of Zn^{2+} ions at 298.15 K, another multi-step run using NVT ensemble with static electric fields in z-direction of 0.1, 0.5, 1 and 2 V/nm for each 10 ns was conducted, which was then followed by final production run in NVT ensemble for 100 ns (Supplementary Figs. 47–49, Supplementary Table 3).

Transference number: The transference number ($t_{Zn^{2+}}$) is defined as the ratio of the current carried by target ions to the total ionic current carried by all the charge species. To measure $t_{Zn^{2+}}$, the Bruce-Vincent method was used. Typically, Zn|CZHE|Zn and Zn|LE|Zn symmetric cells were assembled. In order to improve the quality of experimental data and minimize the impact of interface instability on test results, the cell was first stabilized in the oven for at least 12 h, then cycled at a low current density of 0.1 mA cm^{-2} for several cycles, till a consistent overpotential value of each cycle is obtained. Next, a constant voltage of 5 mV was applied to the cell. Then, the resultant current decay profile as a function of time was recorded till a steady-state reached. Before and after the polarization, EIS was performed to determine the interfacial resistance, and $t_{Zn^{2+}}$ was calculated via the following equation: [67,68]

$$t_{Zn^{2+}} = \frac{I_{ss}(\Delta V - I_0 R_0)}{I_0(\Delta V - I_{ss} R_{ss})} \tag{6}$$

where I_0 and I_{ss} are the initial and steady-state currents, respectively, R_0 and R_{ss} are the interfacial resistances before and after direct current (DC) polarization (obtained from EIS), ΔV is the applied DC bias (typically 5 mV in our case).

Dielectric Loss: EIS measurements were performed using a symmetric two-electrode configuration. The electrolyte sample-either the CZHE or the LE-was sandwiched between two titanium (Ti) foils, which acted as blocking electrodes to prevent faradaic reactions and ensure that the impedance response is dominated by ionic processes. The measurements were conducted at 25 °C over a frequency range from 1 Hz to 1 × 10^5 Hz, using an AC voltage amplitude of 5 mV.

The dielectric loss ε", which reflects the energy dissipation associated with ion movement and interfacial polarization, was computed

using the following equation: [69]

$$\epsilon'' = \frac{Z'}{\omega \cdot C_0 \cdot |Z|^2} \tag{7}$$

Where Z' is the real impedance component,

$\omega = 2\pi f$ is the angular frequency,

$C_0 = \varepsilon_0 \cdot \frac{A}{d}$ is geometrical capacitance determined by the electrode area and electrolyte thickness. The vacuum permittivity ε_0 is $8.854 \times 10^{-12} \mathrm{F} m^{-1}$.

From the EIS measurements, the real (Z') and imaginary (Z'') components of impedance were extracted at each frequency. The total impedance magnitude was calculated as:

$$|Z| = \sqrt{Z'^2 + Z''^2} \tag{8}$$

Mean square displacements (MSD): as a function of simulation time were calculated according to the equation (1). [70,71]

$$\mathrm{MSD}(t) = \left\langle \sum_{i=1}^{3} |r_i(t) - r_i(0)|^2 \right\rangle = \frac{1}{N} \sum_{j=1}^{N} \sum_{i=1}^{3} |r_i^j(t) - r_i^j(0)|^2 \tag{9}$$

In which N is the total atom number, $\langle \ldots \rangle$ denotes the average value over all atoms, $r_i(0)$ and $r_i(t)$ are i-axis positions at simulation time 0 and t. The diffusion coefficient was calculated by least squares fitting a straight line (Dt + c) through the MSD(t) within the diffusive region time.

MSD Calculation under External Electric Field

Zn^{2+} drift distance along the z-direction electric field was calculated using the following equation:

$$Drift\ distance(t) = \frac{1}{N} \sum_{i=1}^{N} [z_i(t) - z_i(0)] \tag{10}$$

Where $z_i(t)$ is z-coordinate of ion i at time t, $z_i(0)$ is initial z-coordinate of ion i at $t = 0$.

N is number of Zn^{2+} considered.

Data availability

Data supporting the findings of this work are available within the article and its Supplementary Information file. The calculation data generated in this study are provided in the Supplementary data files. Source data file for the figures has been deposited in Figshare under accession code DOI link. [https://doi.org/10.6084/m9.figshare.30336571].

References

1. Dubal, D. P., Chodankar, N. R., Kim, D. H. & Gomez-Romero, P. Towards flexible solid-state supercapacitors for smart and wearable electronics. *Chem. Soc. Rev.* **47**, 2065–2129 (2018).
2. Chao, D. et al. Roadmap for advanced aqueous batteries: From design of materials to applications. *Sci. Adv.* **6**, eaba4098 (2020).
3. Liang, Y. & Yao, Y. Designing modern aqueous batteries. *Nat. Rev. Mater.* **8**, 109–122 (2023).
4. Liu, S. et al. Zinc ion batteries: bridging the gap from academia to industry for grid-scale energy storage. *Angew. Chem. Int. Ed. Engl.* **63**, e202400045 (2024).
5. Zhang, H., Liu, X., Li, H., Hasa, I. & Passerini, S. Challenges and strategies for high-energy aqueous electrolyte rechargeable batteries. *Angew. Chem. Int. Ed.* **60**, 598–616 (2021).
6. Wang, Z. et al. Hydrogel electrolytes for flexible aqueous energy storage devices. *Adv. Funct. Mater.* **28**, 1804560 (2018).
7. Wu, K. et al. Recent advances in polymer electrolytes for zinc ion batteries: mechanisms, properties, and perspectives. *Adv. Energy Mater.* **10**, 1903977 (2020).
8. Wang, C. et al. Rechargeable zinc-air batteries with neutral electrolytes: recent advances, challenges, and prospects. *EnergyChem* **3**, 100055 (2021).
9. Liu, S. et al. From room temperature to harsh temperature applications: Fundamentals and perspectives on electrolytes in zinc metal batteries. *Sci. Adv.* **8**, eabn5097 (2022).
10. Wang, F. et al. Highly reversible zinc metal anode for aqueous batteries. *Nat. Mater.* **17**, 543–549 (2018).
11. Jiang, H. et al. Chloride electrolyte enabled practical zinc metal battery with a near-unity Coulombic efficiency. *Nat. Sustain.* **6**, 806–815 (2023).
12. Suo, L. et al. Water-in-salt" electrolyte enables high-voltage aqueous lithium-ion chemistries. *Science* **350**, 938–943 (2015).
13. Xie, J., Liang, Z. & Lu, Y. C. Molecular crowding electrolytes for high-voltage aqueous batteries. *Nat. Mater.* **19**, 1006–1011 (2020).
14. Wang, C. et al. Salt-tolerance training enabled flexible molten hydrate gel electrolytes for energy-dense and stable zinc storage. *Matter* **6**, 3993–4012 (2023).
15. Khan, Z., Kumar, D. & Crispin, X. Does water-in-salt electrolyte subdue issues of Zn batteries?. *Adv. Mater.* **35**, 2300369 (2023).
16. Wu, Z. et al. Unveiling the mysteries: acetonitrile's dance with weakly-solvating electrolytes in shaping gas evolution and electrochemical performance of zinc-ion batteries. *Angew. Chem. Int. Ed.* **63**, e202402206 (2024).
17. Guo, Y. et al. Hydrogels and hydrogel-derived materials for energy and water sustainability. *Chem. Rev.* **120**, 7642–7707 (2020).
18. Zhu, T. et al. Recent advances in conductive hydrogels: classifications, properties, and applications. *Chem. Soc. Rev.* **52**, 473–509 (2023).
19. Li, G. et al. A biocompatible electrolyte enables highly reversible Zn anode for zinc ion battery. *Nat. Commun.* **14**, 6526 (2023).
20. Wang, Y. et al. Lean-water hydrogel electrolyte for zinc ion batteries. *Nat. Commun.* **14**, 3890 (2023).
21. Tiyapiboonchaiya, C. et al. The zwitterion effect in high-conductivity polyelectrolyte materials. *Nat. Mater.* **3**, 29–32 (2004).
22. Peng, X. et al. A zwitterionic gel electrolyte for efficient solid-state supercapacitors. *Nat. Commun.* **7**, 1–8 (2016).
23. Makhlooghiazad, F. et al. Zwitterionic materials with disorder and plasticity and their application as non-volatile solid or liquid electrolytes. *Nat. Mater.* **21**, 228–236 (2022).
24. Jin, S. et al. Zwitterionic polymer gradient interphases for reversible zinc electrochemistry in aqueous alkaline electrolytes. *J. Am. Chem. Soc.* **144**, 19344–19352 (2022).
25. Bi, H. et al. A universal approach to aqueous energy storage via ultralow-cost electrolyte with super-concentrated sugar as hydrogen-bond-regulated solute. *Adv. Mater.* **32**, 2000074 (2020).
26. Han, Z. et al. A versatile hydrogel network repairing strategy achieved by the covalent-like hydrogen bond interaction. *Sci. Adv.* **8**, eabl5066 (2022).
27. Zhou, X., Zhao, F., Guo, Y., Rosenberger, B. & Yu, G. Architecting highly hydratable polymer networks to tune the water state for solar water purification. *Sci. Adv.* **5**, eaaw5484 (2019).
28. Patel, M. B., Agarwal, A. & Bist, H. D. Single crystal Raman spectra of magnesium and zinc perchlorate hexahydrates. *J. Raman Spectrosc.* **14**, 406–409 (1983).
29. Zhang, Y.-H. & Chan, C. K. Observations of water monomers in supersaturated NaClO4, LiClO4, and Mg(ClO4)2 droplets using Raman spectroscopy. *J. Phys. Chem. A* **107**, 5956–5962 (2003).
30. Rodgers, G. E. & Plane, R. A. A Raman spectrophotometric study of the effect of N, N-dimethylformamide and the electrolytes NaClO4, Zn (ClO4) 2, NaNO3, and Zn (NO3) 2 on the structure of liquid water. *J. Chem. Phys.* **63**, 818–829 (1975).
31. Huang, S., Hou, L., Li, T., Jiao, Y. & Wu, P. Antifreezing Hydrogel Electrolyte with Ternary Hydrogen Bonding for High-Performance Zinc-Ion Batteries. *Adv. Mater.* **34**, 2110140 (2022).

32. Zhang, Y.-H. & Chan, C. K. Study of contact ion pairs of supersaturated magnesium sulfate solutions using Raman scattering of levitated single droplets. *J. Phys. Chem. A* **104**, 9191–9196 (2000).
33. Ming, F. et al. Co-solvent electrolyte engineering for stable anode-free zinc metal batteries. *J. Am. Chem. Soc.* **144**, 7160–7170 (2022).
34. Wang, D. et al. Solvation modulation enhances anion-derived solid electrolyte interphase for deep cycling of aqueous zinc metal batteries. *Angew. Chem. Int. Ed.* **62**, e202310290 (2023).
35. Luo, J. et al. Regulating the inner helmholtz plane with a high donor additive for efficient anode reversibility in aqueous Zn-Ion batteries. *Angew. Chem. Int. Ed.* **62**, e202302302 (2023).
36. Liu, T. et al. Aqueous electrolyte with weak hydrogen bonds for four-electron zinc–iodine battery operates in a wide temperature range. *Adv. Mater.* **36**, 2405473 (2024).
37. Maciel, G. E., Simeral, L. & Ackerman, J. J. Effect of complexation of zinc (II) on zinc-67 chemical shifts. *J. Phys. Chem.* **81**, 263–267 (1977).
38. Han, Z. et al. A versatile hydrogel network–repairing strategy achieved by the covalent-like hydrogen bond interaction. *Sci. Adv.* **8**, eabl5066 (2022).
39. Wan, H., Xu, J. & Wang, C. Designing electrolytes and interphases for high-energy lithium batteries. *Nat. Rev. Chem.* **8**, 30–44 (2024).
40. Lu, C. et al. Dehydration-enhanced ion-pore interactions dominate anion transport and selectivity in nanochannels. *Sci. Adv.* **9**, eadf8412 (2023).
41. Sun, S. et al. Eliminating interfacial O-involving degradation in Li-rich Mn-based cathodes for all-solid-state lithium batteries. *Sci. Adv.* **8**, eadd5189 (2022).
42. Nan, B. et al. Enhancing Li+ transport in NMC811|| graphite lithium-ion batteries at low temperatures by using low-polarity-solvent electrolytes. *Angew. Chem. Int. Ed.* **61**, e202205967 (2022).
43. Hong, H. et al. Metal-free eutectic electrolyte with weak hydrogen bonds for high-rate and ultra-stable ammonium-ion batteries. *Adv. Mater.* **36**, 2308210 (2024).
44. Lu, Y., Zhao, C.-Z., Huang, J.-Q. & Zhang, Q. The timescale identification decoupling complicated kinetic processes in lithium batteries. *Joule* **6**, 1172–1198 (2022).
45. Yu, X. et al. Ten concerns of Zn metal anode for rechargeable aqueous zinc batteries. *Joule* **7**, 1145–1175 (2023).
46. Zhang, R. et al. Weakly solvating aqueous-based electrolyte facilitated by a soft co-solvent for extreme temperature operations of zinc-ion batteries. *Energy Environ. Sci.* **17**, 4569–4581 (2024).
47. Mao, L. et al. Functional hydrogels for aqueous zinc-based batteries: progress and perspectives. *Adv. Mater.* e2416345 (2024).
48. Wang, C., Zeng, X., Cullen, P. J. & Pei, Z. The rise of flexible zinc-ion hybrid capacitors: advances, challenges, and outlooks. *J. Mater. Chem. A* **9**, 19054–19082 (2021).
49. Wang, C. et al. Toward flexible zinc-ion hybrid capacitors with superhigh energy density and ultralong cycling life: the pivotal role of ZnCl2 salt-based electrolytes. *Angew. Chem. Int. Ed.* **60**, 990–997 (2021).
50. Leong, K. W. et al. Next-generation magnesium-ion batteries: The quasi-solid-state approach to multivalent metal ion storage. *Sci. Adv.* **9**, eadh1181 (2023).
51. Ge, K., Shao, H., Raymundo-Piñero, E., Taberna, P.-L. & Simon, P. Cation desolvation-induced capacitance enhancement in reduced graphene oxide (rGO). *Nat. Commun.* **15**, 1935 (2024).
52. Kresse, G. & Hafner, J. Ab initio molecular dynamics for liquid metals. *Phys. Rev. B* **47**, 558–561 (1993).
53. Kresse, G. & Furthmüller, J. Efficient iterative schemes for ab initio total-energy calculations using a plane-wave basis set. *Phys. Rev. B* **54**, 11169–11186 (1996).
54. Perdew, J. P., Burke, K. & Ernzerhof, M. Generalized gradient approximation made simple. *Phys. Rev. Lett.* **77**, 3865–3868 (1996).
55. Kresse, G. & Joubert, D. From ultrasoft pseudopotentials to the projector augmented-wave method. *Phys. Rev. B* **59**, 1758–1775 (1999).
56. Blöchl, P. E. Projector augmented-wave method. *Phys. Rev. B* **50**, 17953–17979 (1994).
57. Liechtenstein, A. I., Anisimov, V. I. & Zaanen, J. Density-functional theory and strong interactions: orbital ordering in Mott-Hubbard insulators. *Phys. Rev. B* **52**, R5467–R5470 (1995).
58. Grimme, S. Semiempirical GGA-type density functional constructed with a long-range dispersion correction. *J. Comput. Chem.* **27**, 1787–1799 (2006).
59. Wang, J., Wolf, R. M., Caldwell, J. W., Kollman, P. A. & Case, D. A. Development and testing of a general amber force field. *J. Comput. Chem.* **25**, 1157–1174 (2004).
60. Sousa da Silva, A. W. & Vranken, W. F. ACPYPE - AnteChamber PYthon Parser interfacE. *BMC Res. Notes* **5**, 367 (2012).
61. Parrinello, M. & Rahman, A. Polymorphic transitions in single crystals: a new molecular dynamics method. *J. Appl. Phys.* **52**, 7182–7190 (1981).
62. Nosé, S. A unified formulation of the constant temperature molecular dynamics methods. *J. Chem. Phys.* **81**, 511–519 (1984).
63. Matsumoto, M., Saito, S. & Ohmine, I. Molecular dynamics simulation of the ice nucleation and growth process leading to water freezing. *Nature* **416**, 409–413 (2002).
64. Qiu, M. et al. Tailoring water structure with high-tetrahedral-entropy for antifreezing electrolytes and energy storage at −80 °C. *Nat. Commun.* **14**, 601 (2023).
65. Gowers, R. J. et al. *MDAnalysis: a Python package for the rapid analysis of molecular dynamics simulations*. Report No. 2575-9752, (Los Alamos National Laboratory (LANL), Los Alamos, NM (United States), 2019).
66. Michaud-Agrawal, N., Denning, E. J., Woolf, T. B. & Beckstein, O. MDAnalysis: a toolkit for the analysis of molecular dynamics simulations. *J. Comput. Chem.* **32**, 2319–2327 (2011).
67. Zugmann, S. et al. Measurement of transference numbers for lithium ion electrolytes via four different methods, a comparative study. *Electrochim. Acta.* **56**, 3926–3933 (2011).
68. Chen, F., Wang, X., Armand, M. & Forsyth, M. Cationic polymer-in-salt electrolytes for fast metal ion conduction and solid-state battery applications. *Nat. Mater.* **21**, 1175–1182 (2022).
69. McKubre, M. C. H., Macdonald, D. D., Sayers, B. & Macdonald, J. R. in *Impedance Spectroscopy* 107–174 (2018).
70. Lu, D. et al. Ligand-channel-enabled ultrafast Li-ion conduction. *Nature* **627**, 101–107 (2024).
71. Zhou, S. et al. Visualizing interfacial collective reaction behaviour of Li–S batteries. *Nature* **621**, 75–81 (2023).

Acknowledgements

This work was financially support by Australian Research Council (DE200101669 Z.P., FL210100050 Z.Guo, IH200100035 Z.Guo). The authors acknowledge the high-performance computing support from National Computational Infrastructure (NCI) Australia. Z.P. also acknowledges University of Sydney Horizon Fellowship.

Author contributions

C.W., Z.Guo and Z.P. conceived the idea, designed the experiment, and the project. C.W., Z.Gong and Z.P. fabricated the batteries, performed characterizations and analyzed the data. J.A.Y., Q.M. performed the simulations and calculations. C.W. wrote the initial manuscript. Y.L., S.Z., S.X., X.Z. and P.J.C. participated in discussing the data and commented on the manuscript. J.M., Z.Guo and Z.P. revised the manuscript. All authors approved the manuscript.

Competing interests

The authors declare no competing interests.

Additional information

Supplementary information The online version contains supplementary material available at https://doi.org/10.1038/s41467-025-66041-y.

Correspondence and requests for materials should be addressed to Jianfeng Mao, Zaiping Guo or Zengxia Pei.

Peer review information *Nature Communications* thanks Qiang Hu, Kothandaraman Ramanujam, Jingxin Zhao and the other, anonymous, reviewer(s) for their contribution to the peer review of this work. A peer review file is available.

Reprints and permissions information is available at http://www.nature.com/reprints

Publisher's note Springer Nature remains neutral with regard to jurisdictional claims in published maps and institutional affiliations.

Open Access This article is licensed under a Creative Commons Attribution-NonCommercial-NoDerivatives 4.0 International License, which permits any non-commercial use, sharing, distribution and reproduction in any medium or format, as long as you give appropriate credit to the original author(s) and the source, provide a link to the Creative Commons licence, and indicate if you modified the licensed material. You do not have permission under this licence to share adapted material derived from this article or parts of it. The images or other third party material in this article are included in the article's Creative Commons licence, unless indicated otherwise in a credit line to the material. If material is not included in the article's Creative Commons licence and your intended use is not permitted by statutory regulation or exceeds the permitted use, you will need to obtain permission directly from the copyright holder. To view a copy of this licence, visit http://creativecommons.org/licenses/by-nc-nd/4.0/.

© The Author(s) 2025